

Sub-10 nm Fe₃O₄@Cu_{2-x}S Core–Shell Nanoparticles for Dual-Modal Imaging and Photothermal Therapy

Qiwei Tian,[†] Junqing Hu,^{*,†} Yihan Zhu,[‡] Rujia Zou,[†] Zhigang Chen,[†] Shiping Yang,[§] Runwei Li,^{||} Qianqian Su,[⊥] Yu Han,[‡] and Xiaogang Liu^{*,⊥,#}

[†]State Key Laboratory for Modification of Chemical Fibers and Polymer Materials, College of Materials Science and Engineering, Donghua University, Shanghai 201620, China

[‡]Advanced Membranes and Porous Materials Center, Chemical and Life Science and Engineering Division, King Abdullah University of Science and Technology, Thuwal 23955-6900, Saudi Arabia

[§]Department of Chemistry, Shanghai Normal University, Shanghai 200234, China

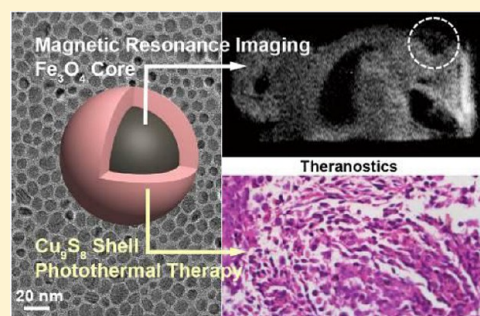
^{||}Key Laboratory of Magnetic Materials and Devices, Ningbo Institute of Materials Technology and Engineering, Chinese Academy of Sciences, Ningbo, Zhejiang, 315201

[⊥]Department of Chemistry, National University of Singapore, 3 Science Drive 3, Singapore 117543, Singapore

[#]Institute of Material Research and Engineering, 3 Research Link, Singapore 117602, Singapore

Supporting Information

ABSTRACT: Photothermal nanomaterials have recently attracted significant research interest due to their potential applications in biological imaging and therapeutics. However, the development of small-sized photothermal nanomaterials with high thermal stability remains a formidable challenge. Here, we report the rational design and synthesis of ultrasmall (<10 nm) Fe₃O₄@Cu_{2-x}S core–shell nanoparticles, which offer both high photothermal stability and superparamagnetic properties. Specifically, these core–shell nanoparticles have proven effective as probes for T₂-weighted magnetic resonance imaging and infrared thermal imaging because of their strong absorption at the near-infrared region centered around 960 nm. Importantly, the photothermal effect of the nanoparticles can be precisely controlled by varying the Cu content in the core–shell structure. Furthermore, we demonstrate *in vitro* and *in vivo* photothermal ablation of cancer cells using these multifunctional nanoparticles. The results should provide improved understanding of synergistic effect resulting from the integration of magnetism with photothermal phenomenon, important for developing multimode nanoparticle probes for biomedical applications.



INTRODUCTION

Nanoparticles with combined magnetic and optical functionalities are important for biomedical applications.¹ Such multifunctional nanoparticles allow for simultaneous diagnostics, therapeutics, and monitoring of response to treatment, offering the potential for reducing common chemotherapy- or radiation-associated side effects and increasing the effectiveness of therapy. In particular, nanoparticles that exhibit both magnetism and near-infrared (NIR) absorption are now being actively investigated for a synergistic effect.² Magnetic component enhances the capacity of nanoparticles as contrast agents for magnetic resonance imaging (MRI), which offers high spatial resolution and deep tissue penetration. On the other hand, the ability of the nanoparticles to convert NIR irradiation to heat can enable localized damage to tumor cells. Thus, the combination of magnetic properties and local photothermal effects renders these nanoparticles as promising theragnostic agents.

Conventional nanomaterial candidates featuring photothermal properties are generally based on gold nanocages or

nanorods.³ However, these gold nanocrystals exhibit relatively low thermal stability during prolonged laser irradiation, resulting in different maximum absorptions between *in vitro* and *in vivo* correlation studies. Furthermore, the large sizes (typically >50 nm) of these nanocrystals limit their applicability to *in vivo* biological settings. Another interesting class of nanomaterials with photothermal effects is upconversion nanoparticles,⁴ which are capable of converting 980 nm laser irradiation to heat.⁵ Despite their usefulness, these upconversion nanoparticles, however, have a low thermal conversion efficiency in the NIR spectral region due to their narrow absorption cross sections.⁶

Alternatively, copper-containing semiconductor nanocrystals,⁷ characterized by low production cost, high stability, low toxicity, and high photothermal conversion efficiency (for example, 25.7% for Cu₉S₅ and 22% for Cu_{2-x}Se)^{7b,e} comparable to gold nanostructures (21% for Au nanorods and 13% for Au

Received: February 5, 2013

Published: May 20, 2013

nanoshells),^{7e} provide promising platforms as photothermal agents. We envision that the integration of the copper-containing semiconductors with superparamagnetic iron oxide nanoparticles has potential for dual-modal imaging and photothermal treatment of cancers with improved therapeutic effects. Herein, we report the rational design and synthesis of monodisperse Fe₃O₄@Cu_{2-x}S core-shell nanoparticles of sub-10 nm. We also demonstrate the use of these hybrid nanoparticles as ideal multifunctional probes for MRI imaging, infrared thermal imaging, and photothermal ablation of cancer cells.

EXPERIMENTAL SECTION

General. The chemicals of iron(III) acetylacetonate (99%), copper(II) acetylacetonate (98%), and oleylamine (C18 content 80–90%) were purchased from Acros. Sulfur (99.99%), *N*-methyl-2-pyrrolidone, chloroform, and ethanol were purchased from Sinopharm Chemical Reagent Co., Ltd. (Shanghai, China). Hydrolyzed polymaleic anhydride (molecular weight: 400–800) was received from Shandong Taihe Water Treatment Co., Ltd. All the chemicals were used without further purification.

Synthesis of Fe₃O₄ Nanoparticles. Fe₃O₄ nanocrystals were synthesized by a modified literature procedure.⁸ In a typical procedure, 15 mL of oleylamine was slowly heated to 300 °C in a round-bottom flask while stirring for 30 min. The flask was purged with dry nitrogen gas to remove residual water and oxygen. Subsequently, a solution containing 3 mL of oleylamine, 2 mL of *N*-methyl-2-pyrrolidone, and 0.5 mmol of Fe(acac)₃ was injected into the hot flask, resulting in an immediate dark color. After been kept at 300 °C for 10 min, the solution was slowly cooled down to 60 °C. An ethanol solution (30 mL) was then added to the reaction mixture, affording a black precipitate. The nanoparticle product was collected by centrifugation, washed with ethanol, and redispersed in 20 mL of chloroform prior to use.

Synthesis of Fe₃O₄@Cu_{2-x}S Core-Shell Nanoparticles. To grow a thin layer of Cu_{2-x}S shell onto Fe₃O₄ nanoparticles, 1 mmol of S dissolved in 3 mL of oleylamine was rapidly injected into a cyclohexane solution (10 mL) of the as-synthesized Fe₃O₄ nanoparticles at 70 °C and stirred at this temperature for 10 min. To this solution was then injected 0.5 mmol of Cu(acac)₂ dissolved in 4 mL of chloroform solution and 1 mL of oleylamine. The resulting mixture was kept at 70 °C for another 30 min, at which time the color of the solution gradually turned dark green. The oleylamine-capped Fe₃O₄@Cu_{2-x}S nanoparticles were collected by centrifugation and washed twice with ethanol and chloroform, successively. The preparation of MFe₂O₄@Cu_{2-x}S (M = Co and Ni) core-shell nanoparticles was carried out in a similar procedure to that for Fe₃O₄@Cu_{2-x}S nanoparticles. Note that CoCl₂ and NiCl₂ precursors were used in combination with Fe(acac)₃ in a 1:2 mol ratio to synthesize CoFe₂O₄ and NiFe₂O₄, respectively.

Synthesis of Polymer-Modified Fe₃O₄@Cu_{2-x}S Nanoparticles. The as-prepared Fe₃O₄@Cu_{2-x}S nanoparticles were coated with an amphiphilic hydrolyzed polymaleic anhydride premodified with oleylamine according to a literature report.⁹ To a 50 mL round-bottom flask was added 0.5 mM of monomer units (dissolved in 5 mL of chloroform and 5 mL of ethanol) and 200 mg of oleylamine-capped Fe₃O₄@Cu_{2-x}S nanoparticles (dissolved in 10 mL of chloroform). The resulting mixture was stirred for 30 min. Subsequent rotary evaporation of the solvent resulted in a dark-green film of polymer-coated core-shell nanoparticles attached to the inner wall of the flask. Ten mL of aqueous sodium borate buffer (SBB, pH 12) was then added to the flask and subject to ultrasonication for 15 min. After phase transfer from chloroform to aqueous solution, the hydrophilic Fe₃O₄@Cu_{2-x}S core-shell nanoparticles were collected by using a magnet. The aqueous solution of the core-shell nanoparticles was stored in a glass vial under ambient conditions before being used in MRI and photothermal therapy studies.

In vivo MRI Studies. MRI *in vivo* was performed with a 0.5T MiniMR-60 MRI system (Shanghai Niumag Corporation). The use and operation of nude mice with body weight of ~14 g were approved by the institute's animal care and use committee. The mouse was anaesthetized by trichloroacetaldehyde hydrate (10%) at a dosage of 40 mg/kg body weight and maintained at normal body temperature. Subsequently, the polymer-coated Fe₃O₄@Cu_{2-x}S (100 μL) nanoparticles (20 ppm Fe) in phosphate-buffered saline (PBS) were injected to the back of the mouse through hypodermic injection. Transversal cross-sectional scan images were taken before and 1 h after the particle administration for MRI analysis.

Measurement of Photothermal Performance. To measure the photothermal conversion performance of hydrophilic Fe₃O₄@Cu_{2-x}S core-shell nanoparticles, a 980 nm NIR laser was used to excite the nanoparticles through a quartz cuvette containing an aqueous dispersion (0.3 mL) of the hydrophilic nanoparticles with different concentrations (3.13, 6.25, 12.5, 25, and 50 ppm). The NIR light source was equipped with an external adjustable power (0–2 W/cm²) and a 5-mm diameter laser module (Xi'an Tours Radium Hirsh Laser Technology Co., Ltd. China). The output power, calibrated using a handy optical power meter (Newport model 1918-C, CA, U.S.A.), was found to be ~0.6 W/cm². The temperature was recorded by an online-type thermocouple thermometer (DT-8891E Shenzhen Everbest Machinery Industry Co., Ltd, China) with an accuracy of ±0.1 °C.

To evaluate the photothermal conversion efficiency, the temperature change of the aqueous dispersion (50 ppm) was recorded as a function of time under continuous irradiation of the 980 nm laser with a power density of 0.6 W/cm² until the solution reached a steady-state temperature. The photothermal conversion efficiency, η , was calculated using eq 1 described by Roper:¹⁰

$$\eta = \frac{hS(T_{\max} - T_{\text{Surr}}) - Q_{\text{Dis}}}{I(1 - 10^{-A_{980}})} \quad (1)$$

where h is the heat transfer coefficient, S is the surface area of the container, T_{\max} is the equilibrium temperature, T_{Surr} is ambient temperature of the surroundings, Q_{Dis} expresses the heat dissipation from the light absorbed by the quartz sample cell, I is incident laser power (600 mW/cm²), and A_{980} is the absorbance of the Fe₃O₄@Cu_{2-x}S nanoparticles at 980 nm. The value of hS is derived according to eq 2:

$$\tau_s = \frac{m_D C_D}{hS} \quad (2)$$

where τ_s is the sample system time constant, m_D and C_D are the mass (0.3 g) and heat capacity (4.2 J/g) of deionized water used as the solvent, respectively. The Q_{Dis} (25.7 mW) was measured independently using a quartz cuvette cell containing pure water without the nanoparticles.

Photothermal Ablation of Cancer Cells *in Vitro*. HeLa cells were plated in a 24-well plate at a density of 15 000 cells/mL in DMEM at 37 °C in the presence of 5% CO₂ for 24 h prior to treatment. After 24 h of incubation, the DMEM was taken out from the wells, and the cells were washed for three times with a PBS solution. The polymer-modified Fe₃O₄@Cu_{2-x}S core-shell nanoparticles dispersed in a PBS solution were then added into the wells. The cells were irradiated for 4 min using a 980 nm laser with an output power density of 0.6 W/cm². Subsequently, the PBS dispersion of the Fe₃O₄@Cu_{2-x}S nanoparticles was removed, and the remaining cells were washed with the PBS solution for three times. A solution of 0.4% trypan blue dye was then added to the wells. After staining for 3 min, the trypan blue was washed with the PBS solution for three times. The dye-treated cells were visualized immediately using an inverted biological microscope (XSP-18CE, Shanghai Changfang Optical Instrument Co., Ltd.). Each experiment was repeated twice.

In vivo Infrared Thermal Imaging Studies. Infrared thermal imaging *in vivo* was performed with a photothermal therapy-monitoring system GX-A300 (Shanghai Guixin Corporation). The tumor-bearing mouse was first anaesthetized using trichloroacetaldehyde hydrate (10%) at a dosage of 40 mg/kg body weight while

maintaining at normal body temperature. The hydrophilic core–shell nanoparticles (100 μL) in PBS buffer (50 ppm Cu) were then injected to the tumor of the mouse through intratumoral injection. The spatial temperature distributions of the nanoparticles were recorded under the 980 nm laser irradiation.

Photothermal Ablation of Cancer Cells *in Vivo*. The tumor-bearing (~ 10 mm) mice were randomly allocated into two groups (control and treatment groups). The mice in the treatment group were injected with polymer-modified $\text{Fe}_3\text{O}_4@Cu_{2-x}S$ nanoparticles in PBS buffer (100 μL ; Cu content: 50 ppm) into the tumor site located at a depth of ~ 4 mm, while the tumor-bearing mice in the control group were only injected with PBS buffer. After 1 h, the injected sites from both groups were irradiated with a 980 nm laser (0.6 W/cm^2) for 10 min. The tumor-bearing mice were killed 1 day after the laser treatment. The tumors were removed, embedded in paraffin, and cryosectioned into 4 μm slices. The slides were stained with hematoxylin/eosin and examined under a Zeiss Axiovert 40 CFL inverted fluorescence microscope. The images were captured by a Zeiss AxioCam MRC5 digital camera.

RESULTS AND DISCUSSION

Uniform spherical-shaped Fe_3O_4 nanoparticles were synthesized in oleylamine by a modified literature method.⁸ An excess of sulfur was then added to the magnetic nanoparticles to afford $\text{Fe}_3\text{O}_4@S$ core–shell nanoparticles (Figures 1a and S1).¹¹ Subsequently, the sulfur-coated magnetic nanoparticles were

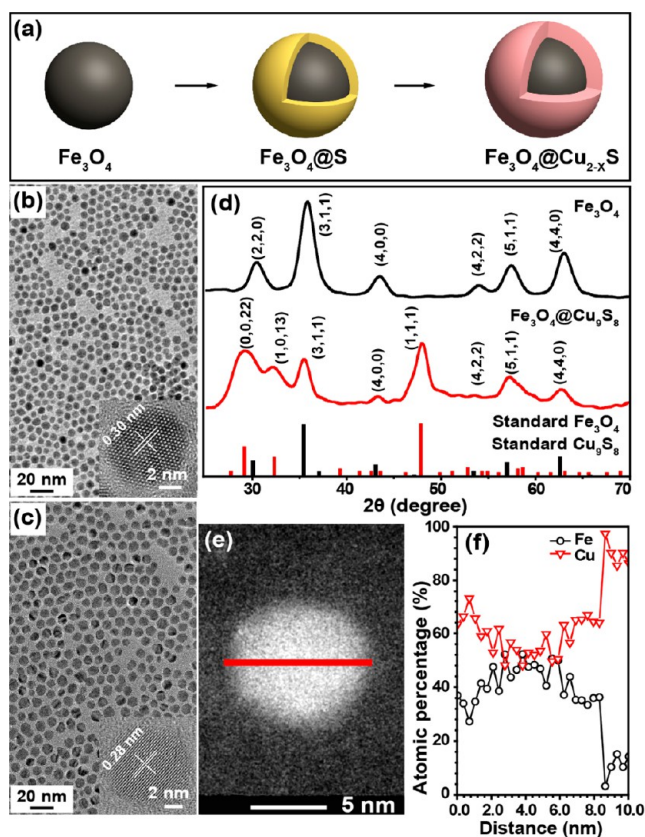


Figure 1. (a) Experimental design for the synthesis of $\text{Fe}_3\text{O}_4@Cu_{2-x}S$ core–shell nanostructures. (b,c) TEM images of the as-synthesized Fe_3O_4 and $\text{Fe}_3\text{O}_4@Cu_{2-x}S$ nanoparticles and the corresponding high-resolution micrographs (Insets). (d) Powder X-ray diffraction patterns of the Fe_3O_4 and $\text{Fe}_3\text{O}_4@Cu_{2-x}S$ nanoparticles, as referenced by standard Fe_3O_4 and Cu_9S_8 phases. (e) STEM image of a single core–shell nanoparticle. (f) The corresponding EDX line scan profiles of the core–shell nanoparticle, indicating a higher Cu concentration in the peripheral region of the crystal.

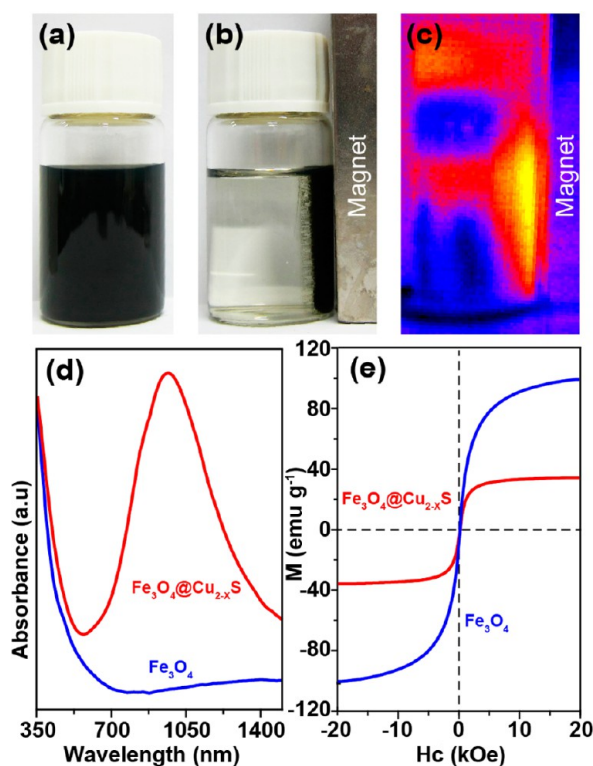


Figure 2. (a,b) Photographs of a chloroform solution of $\text{Fe}_3\text{O}_4@Cu_{2-x}S$ nanoparticles in the absence and presence of a magnet. (c) Infrared thermograph of the core–shell nanoparticles taken in the presence of a magnet and under a 980 nm laser irradiation. Note that the snap cap of the vial also absorbs the laser light due to its polymer content. (d) Corresponding UV–vis–NIR absorption spectra for colloidal solutions of the Fe_3O_4 nanoparticles and $\text{Fe}_3\text{O}_4@Cu_{2-x}S$ nanoparticles dispersed in chloroform. (e) Room-temperature magnetization measurements of the $\text{Fe}_3\text{O}_4@Cu_{2-x}S$ and Fe_3O_4 nanoparticles.

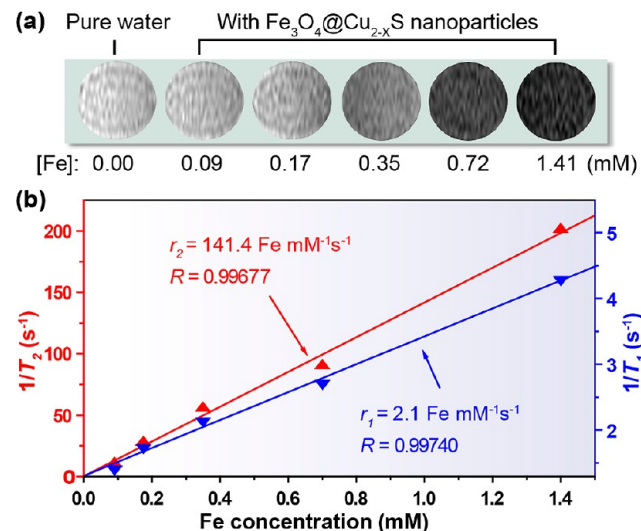


Figure 3. (a) T_2 -weighted MRI photographs of the polymer-modified $\text{Fe}_3\text{O}_4@Cu_{2-x}S$ nanoparticles dispersed in water with different Fe concentrations. (b) Corresponding T_2 relaxation rate ($1/T_2$, red line) and T_1 relaxation rate ($1/T_1$, blue line) of the hydrophilic core–shell nanoparticles as a function of Fe concentration.

treated with copper(II) acetylacetonate dissolved in a mixed solution of oleylamine and chloroform, resulting in the formation of $\text{Fe}_3\text{O}_4@Cu_{2-x}S$ core–shell nanoparticles. It is

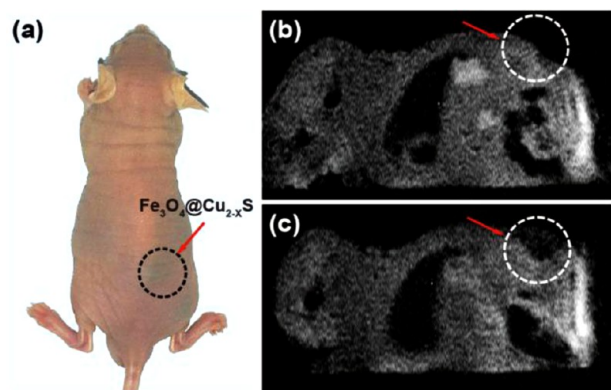


Figure 4. (a) Photograph of the nude mouse injected with the $\text{Fe}_3\text{O}_4@Cu_{2-x}\text{S}$ nanoparticles. The injection site was marked by a dashed circle. (b,c) Cross-sectional snap shots of T_2 -weighted MRI scan of the nude mouse before and after being injected with the $\text{Fe}_3\text{O}_4@Cu_{2-x}\text{S}$ nanoparticles, respectively.

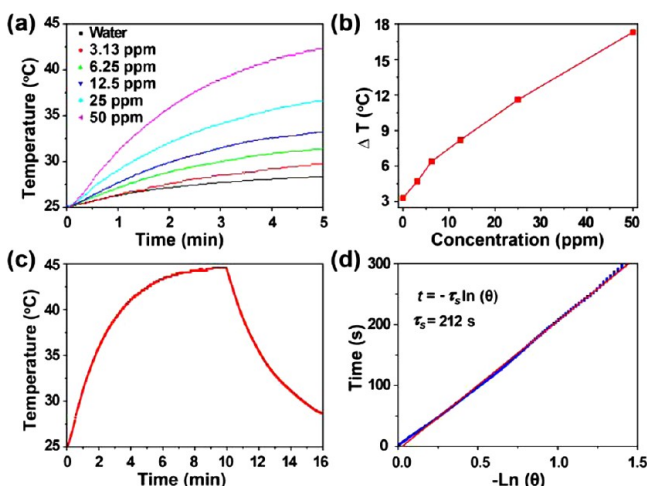


Figure 5. (a) Temperature profiles of pure water and aqueous dispersions of $\text{Fe}_3\text{O}_4@Cu_{2-x}\text{S}$ core-shell nanoparticles at different concentrations determined by the Cu content (3.13, 6.25, 12.5, 25, and 50 ppm) as a function of irradiation time (0–5 min). (b) Plot of temperature change (ΔT) over a period of 5 min versus the Cu concentration. (c) Photothermal effect of an aqueous dispersion of $\text{Fe}_3\text{O}_4@Cu_{2-x}\text{S}$ core-shell nanoparticles (Cu content: 50 ppm) when illuminated with a 980 nm laser (0.6 W/cm^2). The laser was turned off after irradiation for 10 min. (d) Plot of cooling time versus negative natural logarithm of the temperature driving force obtained from the cooling stage as shown in (c). The time constant for heat transfer of the system is determined to be $\tau_s = 212$.

important to note that this method can be readily extended to the synthesis of other types of magnetic copper-containing core-shell nanoparticles, such as $\text{CoFe}_2\text{O}_4@Cu_{2-x}\text{S}$ and $\text{NiFe}_2\text{O}_4@Cu_{2-x}\text{S}$ (Figures S2 and S3).

Typical transmission electron microscope (TEM) images of the as-synthesized Fe_3O_4 and $\text{Fe}_3\text{O}_4@Cu_{2-x}\text{S}$ nanoparticles were shown in Figure 1b,c (or Figure S4). The Fe_3O_4 nanoparticles have an average diameter of 6.5 nm, while the corresponding Cu_{2-x}S -coated nanoparticles have an average size of 8.5 nm. Both samples were examined by X-ray powder diffraction (Figure 1d). The X-ray diffraction pattern of the core-shell sample can be indexed as a mixture of the face-centered cubic Fe_3O_4 (JCPDS file number 65-3107) and hexagonal Cu_9S_8 phases (JCPDS file number 36-0379). The

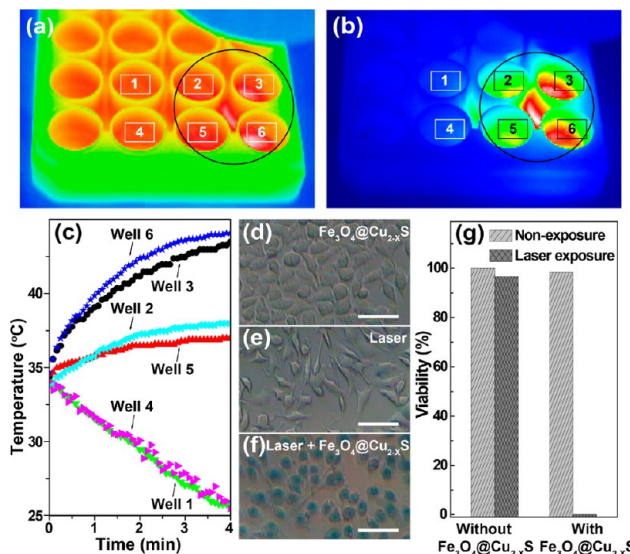


Figure 6. (a,b) Infrared thermographs of a 24-well cell-culture plate before (a) and after (b) laser irradiation (0.6 W/cm^2) for 4 min. The irradiated region is marked by a circle. Note that the culture wells of 1, 3, 4, and 6 contain HeLa cells and the polymer-modified $\text{Fe}_3\text{O}_4@Cu_{2-x}\text{S}$ nanoparticles (50 ppm), while the wells of 2 and 5 contain only HeLa cells. (c) Temperature profiles of the culture wells of 1–6 as a function of laser irradiated time. Note that the wells of 1 and 4 were used as controls without the laser exposure. (d–f) Optical images of HeLa cells incubated in well 1 (d), 2 (e), and 3 (f) obtained after the cell viability (trypan blue) test. Wells 1 and 2 are controls treated with the hydrophilic $\text{Fe}_3\text{O}_4@Cu_{2-x}\text{S}$ nanoparticles and NIR laser, respectively. The laser-ablated killing of HeLa cells in the presence of the core-shell nanoparticles is evident, as shown in panel (f), with the staining of trypan blue. Scale bars for panels (d–f) are $50 \mu\text{m}$. (g) Mortality versus viability quantification for HeLa cells incubated in the culture wells of 1–3.

core-shell nanostructure was further confirmed by energy-dispersive X-ray (EDX) spectroscopic analysis combined with scanning transmission electron microscopy (STEM). We first conducted an EDX line scan measurement on a single core-shell nanoparticle (Figure 1e). The relative concentrations of Fe and Cu along the scanning path were determined and plotted in Figure 1f. The results clearly show that Fe is concentrated in the center region, while Cu shows apparently higher concentration in the periphery region of the particle. We also carried out EDX area scan that provides more signal counts from the periphery region and center region of another nanoparticle (Figure S5). In addition, X-ray photoelectron spectroscopic studies of $\text{Fe}_3\text{O}_4@Cu_{2-x}\text{S}$ nanoparticles confirmed the presence of copper and sulfur (Figure S6). The obtained spectra and the quantitative mapping of the elemental concentration unambiguously point to the core-shell characteristic of the as-synthesized nanoparticles.

We further studied the magnetic and photothermal properties of $\text{Fe}_3\text{O}_4@Cu_{2-x}\text{S}$ nanoparticles. In the presence of a magnet, the nanoparticles dispersed in chloroform can be readily sedimented for isolation (Figure 2a,b). On a 980 nm laser irradiation for 0.5 min, we clearly observed an increase in the temperature of the particle aggregates as measured by infrared thermal imaging (Figure 2c). This can be directly attributed to efficient absorption of NIR light by the Cu_{2-x}S shell. Indeed, the UV-vis absorption spectroscopy of $\text{Fe}_3\text{O}_4@Cu_{2-x}\text{S}$ nanoparticle solutions showed an intense broad band in the range of 700–1400 nm, characteristics of Cu_{2-x}S

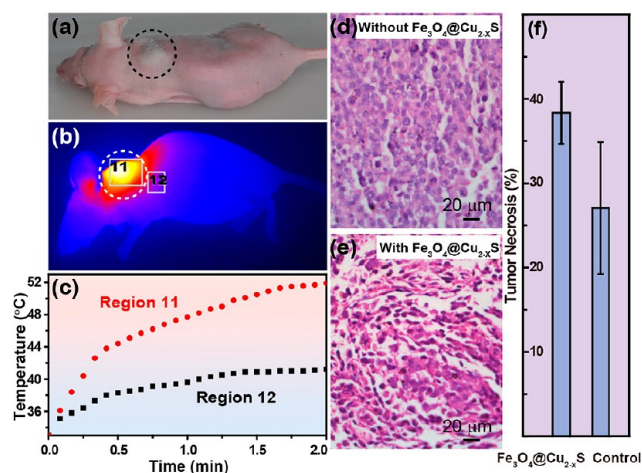


Figure 7. (a) Photograph of the tumor-bearing mouse (marked by a dashed circle). (b) Infrared thermal image of the tumor-bearing mouse treated with the $\text{Fe}_3\text{O}_4@\text{Cu}_{2-x}\text{S}$ nanoparticles after a 980 nm laser irradiation for 2 min. The irradiated area was marked by a dashed circle. Labels 11 and 12 indicate the region with the nanoparticle injection and without the nanoparticle, respectively. (c) The temperature profiles in regions 11 and 12 as a function of the irradiation time. (d,e) The representative hematoxylin and eosin stained histological images of *ex vivo* tumor sections injected with: water only and an aqueous dispersion of polymer-modified $\text{Fe}_3\text{O}_4@\text{Cu}_{2-x}\text{S}$ nanoparticles (Cu content 50 ppm), respectively. (f) Statistical analyses of necrosis in tumors treated with and without $\text{Fe}_3\text{O}_4@\text{Cu}_{2-x}\text{S}$ core-shell nanoparticles (p value: 0.001). The sections were irradiated with the 980 nm laser irradiation for 10 min. Note that the power density is 0.6 W/cm^2 .

nanomaterials due to the localized surface plasmon resonances in vacancy-doped semiconductors.¹² In contrast, Fe_3O_4 nanoparticle solutions did not exhibit any appreciable absorption in that spectral range (Figure 2d). The magnetism of $\text{Fe}_3\text{O}_4@\text{Cu}_{2-x}\text{S}$ nanoparticles was measured by sweeping the external magnetic field between -20 and 20 kOe at room temperature. These core-shell nanoparticles showed no remanence magnetization or coercivity, suggesting that the superparamagnetic nature makes the particles suitable for controlled magnetic manipulation. Notably, the saturated mass magnetization of the Cu_{2-x}S -modified magnetic nanoparticles decreased to a value of 34.1 emu/g relative to 99.7 emu/g for the Fe_3O_4 nanoparticle control, which can be ascribed to the weight contribution from the nonmagnetic Cu_{2-x}S material.

To disperse $\text{Fe}_3\text{O}_4@\text{Cu}_{2-x}\text{S}$ nanoparticles in aqueous solvents for biological applications, we coated the core-shell nanoparticles with an amphiphilic polymer (Figures S7–S9).⁹ The potential of hydrophilic $\text{Fe}_3\text{O}_4@\text{Cu}_{2-x}\text{S}$ nanoparticles as the contrast agents was first examined by using a 0.5-T MRI scanner. Figure 3a shows the magnetic resonance signal-enhancing capability of the core-shell nanoparticles in water as a function of iron concentration. With increased iron concentration, we noticed that the measured T_2 -weighted image contrast gradually darkens. Figure 3b shows the corresponding transverse relaxation ($1/T_2$, red line) and longitudinal relaxation rates ($1/T_1$, blue line) of protons in the particle solution obtained as a function of iron concentration. The calculated r_2 value of $141.4 \text{ mM}^{-1} \text{ s}^{-1}$ is comparable to that of commercial MRI contrast agents (Feridex, $152 \text{ mM}^{-1} \text{ s}^{-1}$; Resovist, $86 \text{ mM}^{-1} \text{ s}^{-1}$)¹² under the same magnetic field intensity. Importantly, the r_2/r_1 ratio (67)

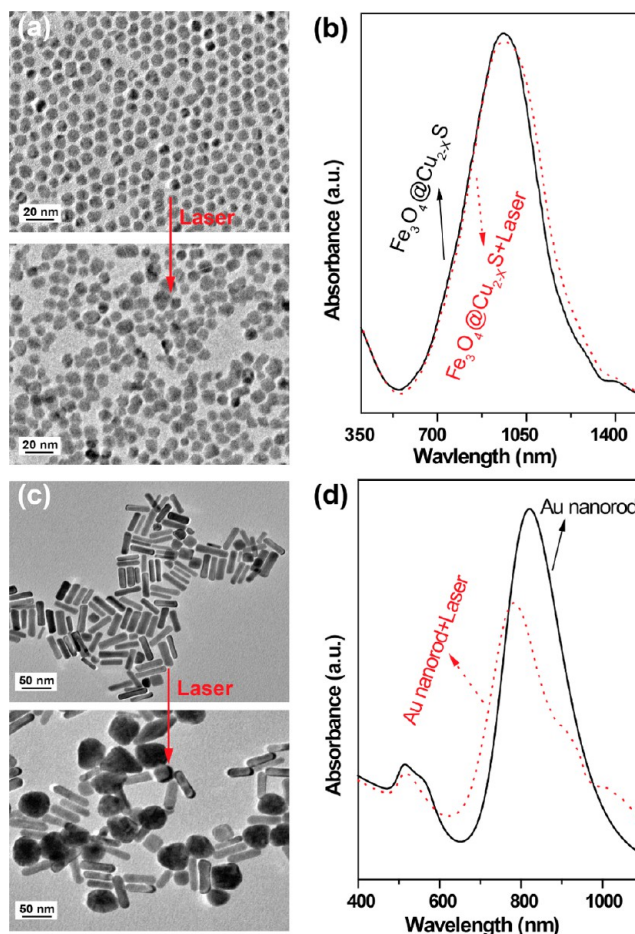


Figure 8. Photothermal stability comparison of (a,b) $\text{Fe}_3\text{O}_4@\text{Cu}_{2-x}\text{S}$ nanoparticles and (c,d) Au nanorods ($50 \times 15 \text{ nm}$) upon irradiation with a 980 nm laser for 30 min (power density: 2 W/cm^2).

of the core-shell nanoparticles is increased by more than 1 order of magnitude when compared to Feridex (5.6) and Resovist (4.3) contrast agents.¹³ For the T_2 -weighted MRI, a high r_2/r_1 value in addition to high r_2 relaxivities enables negative contrast enhancement.¹³

As a proof-of-concept experiment, we evaluated the *in vivo* contrast enhancing effect of the polymer-modified $\text{Fe}_3\text{O}_4@\text{Cu}_{2-x}\text{S}$ nanoparticles in a nude mouse with a 0.5-T MRI scanner. The hydrophilic core-shell nanoparticles were suspended in physiological saline and then injected into the back side ($\sim 0.2 \text{ cm}$ deep) of the mouse with a dosage of 0.14 mg/kg of body weight (Figure 4a). The T_2 -weighted images, recorded before and 1 h after the injection, showed marked negative enhancement of the background tissue at the injection site (Figure 4b,c).

Another important attribute of the hydrophilic $\text{Fe}_3\text{O}_4@\text{Cu}_{2-x}\text{S}$ nanoparticles is their tunable photothermal effect. We first studied the temperature of an aqueous solution loaded with the nanoparticles (Figure 5). Interestingly, the temperature of the solution can be precisely controlled from 25 to $42 \text{ }^\circ\text{C}$ by varying the Cu content (Figure 5a,b). To further study the photothermal performance of the nanoparticles, we recorded the temperature change of the solution (50 ppm) as a function of time under continuous irradiation of the 980 nm laser (0.6 W/cm^2) until the solution reached a steady-state temperature (Figure 5c,d). According to the obtained data (Figures 5c,d and S10), the photothermal conversion efficiency

can reach about 16%. We thus believe that these nanoparticles can be used as excellent contrast agents for infrared thermal imaging, providing an added benefit for real-time monitoring of temperature dynamics of a photothermal therapy process.

To verify our hypothesis, we undertook *in vitro* cytotoxicity test via the methyl thiazolyl tetrazolium (MTT) assay in HeLa cells derived from human cervical carcinoma cell line. The toxicity results showed that the cellular viability was estimated to be higher than 80% after 12 h incubation in the presence of the polymer-modified core–shell nanoparticles with Cu concentrations of 0–100 ppm, indicating a low cytotoxicity within this concentration range (Figure S11). We then explored the infrared thermal imaging and photothermal therapy *in vitro* using HeLa cells incubated in a 24-well plate. As shown in Figure 6, 100 μ L of PBS control each was added into wells 2 and 5, while the PBS dispersion containing 50 ppm of the core–shell nanoparticles was added into the wells 1, 3, 4, and 6, respectively. The laser irradiated areas were marked by the circle (Figure 6a,b; wells 2, 3, 5, and 6). As expected, the nanoparticles exhibit good contrast for infrared thermal imaging (Figure 6b,c). Only the wells containing the core–shell nanoparticles and irradiated with 980 nm laser show high contrast infrared thermal images and obvious temperature elevation (Figure 6, wells 3 and 6). Importantly, we observed efficient photothermal ablation of the HeLa cells only after 4 min irradiation of the 980 nm laser in the presence of the core–shell nanoparticles (Figure 6d–g). Consistent with the trypan blue assay, almost all cancer cells in the wells 3 and 6 died after the laser irradiation. In stark contrast, no obvious cell death was observed for the cells treated with the nanoparticles or directly exposed to the laser alone.

To shed more light on the photothermal effect of the polymer-modified $\text{Fe}_3\text{O}_4@\text{Cu}_{2-x}\text{S}$ nanoparticles, we further performed photothermal effect *in vivo* (Figure S12). Inspiringly, infrared thermal images with high contrast could also be achieved (Figure 7a,b). To further evaluate photothermal ablation of cancer cells *in vivo* by the $\text{Fe}_3\text{O}_4@\text{Cu}_{2-x}\text{S}$ nanoparticles, an aqueous dispersion of the polymer-modified core–shell nanoparticles (Cu content: 50 ppm) was injected intratumorally into a tumor-bearing mouse. Relative to an untreated control with only water injection (Figure 7d), histological examination of the tumors treated with the $\text{Fe}_3\text{O}_4@\text{Cu}_{2-x}\text{S}$ nanoparticles showed typical signs of cell damage under a low-power density laser irradiation (0.6 W/cm²), such as cell shrinkage, loss of contact, and nuclear damage (Figure 7e, also see Figure S13). We further estimated the percentage of necrosis to be \sim 38% in tumors treated with $\text{Fe}_3\text{O}_4@\text{Cu}_{2-x}\text{S}$ nanoparticles and \sim 27% for controls without the nanoparticles (Figure 7f). Taken together, these results unambiguously proof photothermal effects of $\text{Fe}_3\text{O}_4@\text{Cu}_{2-x}\text{S}$ nanoparticles and provide a mechanism for how these particles can contribute to localized killing of cancer cells.

Furthermore, we benchmarked the photothermal stability of the $\text{Fe}_3\text{O}_4@\text{Cu}_{2-x}\text{S}$ nanoparticles with gold (Au) nanorods (50 \times 15 nm) under NIR laser excitation. By analyzing the TEM images taken before and after the laser irradiation (Figure 8), we could clearly observe a higher thermal stability for the $\text{Fe}_3\text{O}_4@\text{Cu}_{2-x}\text{S}$ core–shell nanoparticles than the Au nanorods. The near-infrared absorption spectrum of the core–shell nanoparticle remains essentially unchanged after exposure of the 980 nm laser for 30 min. To exclude the polymer coating effect on the stability of the core–shell nanoparticles, we replaced the polymer coating with cetrimonium bromide

stabilizing molecules (Figures S14 and S15). After six repeated cycles of laser heating, we did not observe any noticeable difference in the thermal conversion efficiency, further confirming high photothermal stability of the $\text{Fe}_3\text{O}_4@\text{Cu}_{2-x}\text{S}$ nanoparticles.

CONCLUSIONS

In conclusion, we present the first successful integration of iron oxide nanoparticles with copper sulfide for the preparation of multifunctional $\text{Fe}_3\text{O}_4@\text{Cu}_{2-x}\text{S}$ core–shell nanomaterials. This new class of nanomaterials features ultrasmall (<10 nm) particle size, superparamagnetic property, low cytotoxicity, and highly efficient photothermal effect. Our investigations point to these nanomaterials as uniquely effective bioprobes for dual-mode imaging and therapy applications, particularly in the treatment of deeply located cancers.

ASSOCIATED CONTENT

Supporting Information

Additional experimental details. This material is available free of charge via the Internet at <http://pubs.acs.org>.

AUTHOR INFORMATION

Corresponding Author

hu.junqing@dh.u.edu.cn; chmlx@nus.edu.sg

Notes

The authors declare no competing financial interest.

ACKNOWLEDGMENTS

This work was partially supported by the National Natural Science Foundation of China (grant nos. 21171035, 50872020, 20971086), Key Grant Project of Chinese Ministry of Education (grant no. 313015), the Science and Technology Commission of Shanghai-based “Innovation Action Plan” Project (grant no. 10JC1400100), and PhD Programs Foundation of Ministry of Education of China (grant no. 20110075110008). X.L. acknowledges the support by the National University of Singapore (R-143-000-427), the Singapore Ministry of Education (R-143-000-453), the Singapore-MIT Alliance, and the Agency for Science, Technology, and Research (R-143-000-366). Y.H. acknowledges the support by the King Abdullah University of Science and Technology for the baseline research funds.

REFERENCES

- (1) (a) Ho, D.; Sun, X.; Sun, S. *Acc. Chem. Res.* **2011**, *44*, 875. (b) Jin, Y.; Jia, C.; Huang, S. W.; O'Donnell, M.; Gao, X. *Nat. Commun.* **2010**, *1*, 41. (c) Gao, J.; Gu, H.; Xu, B. *Acc. Chem. Res.* **2009**, *42*, 1097. (d) Lee, D.-E.; Koo, H.; Sun, I.-C.; Ryu, J. H.; Kim, K.; Kwon, I. C. *Chem. Soc. Rev.* **2012**, *41*, 2656. (e) Kelkar, S. S.; Reineke, T. M. *Bioconjugate Chem.* **2011**, *22*, 1879. (f) Xue, X.; Wang, F.; Liu, X. *J. Mater. Chem.* **2011**, *21*, 13107.
- (2) (a) Sherlock, S. P.; Tabakman, S. M.; Xie, L.; Dai, H. *ACS Nano* **2011**, *5*, 1505. (b) Bardhan, R.; Chen, W.; Perez-Torres, C.; Bartels, M.; Huschka, R. M.; Zhao, L.; Morosan, E. R.; Pautler, G.; Joshi, A.; Halas, N. J. *Adv. Funct. Mater.* **2009**, *19*, 3901. (c) Dong, W.; Li, Y.; Niu, D.; Ma, Z.; Gu, J.; Chen, Y.; Zhao, W.; Liu, X.; Liu, C.; Shi, J. *Adv. Mater.* **2011**, *23*, 5392. (d) Kim, J.; Park, S.; Lee, J. E.; Jin, S. M.; Lee, J. H.; Lee, I. S.; Yang, I.; Kim, J. S.; Kim, S. K.; Cho, M. H.; Hyeon, T. *Angew. Chem., Int. Ed.* **2006**, *45*, 7754. (e) Wang, L.; Bai, J.; Li, Y.; Huang, Y. *Angew. Chem., Int. Ed.* **2008**, *47*, 2439. (f) Melancon, M. P.; Lu, W.; Zhong, M.; Zhou, M.; Liang, G.; Elliott, A. M.; Hazle, J. D.; Myers, J. N.; Li, C.; Stafford, R. J. *Biomaterials* **2011**, *32*, 7600. (g) Ji, X.; Shao, R.; Elliott, A. M.; Stafford, R. J.; Esparza-Coss, E.; Bankson, J.

A.; Liang, G.; Luo, Z.-P.; Park, K.; Markert, J. T.; Li, C. *J. Phys. Chem. C* **2007**, *111*, 6245. (h) Hu, K.-W.; Jhang, F.-Y.; Su, C.-H.; Yeh, C.-S. *J. Mater. Chem.* **2009**, *19*, 2147. (i) Cheng, L.; Yang, K.; Li, Y.; Zeng, X.; Shao, M.; Lee, S.-T.; Liu, Z. *Biomaterials* **2012**, *33*, 2215. (j) Seo, W. S.; Lee, J. H.; Sun, X.; Suzuki, Y.; Mann, D.; Liu, Z.; Terashima, M.; Yang, P.; McConnell, M. V.; Nishimura, D. G.; Dai, H. *Nat. Mater.* **2006**, *5*, 971.

(3) (a) Cobley, C. M.; Chen, J.; Cho, E. C.; Wang, L.; Xia, Y. *Chem. Soc. Rev.* **2011**, *40*, 44. (b) Bardhan, R.; Lal, S.; Joshi, A.; Halas, N. J. *Acc. Chem. Res.* **2011**, *44*, 936. (c) Xia, Y.; Li, W.; Cobley, C. M.; Chen, J.; Xia, X.; Zhang, Q.; Yang, M.; Cho, E. C.; Brown, P. K. *Acc. Chem. Res.* **2011**, *44*, 914. (d) Kennedy, L. C.; Bickford, L. R.; Lewinski, N. A.; Coughlin, A. J.; Hu, Y.; Day, E. S.; West, J. L.; Drezek, R. A. *Small* **2011**, *7*, 169. (e) Dreaden, E. C.; Alkilany, A. M.; Huang, X.; Murphy, C. J.; El-Sayed, M. A. *Chem. Soc. Res.* **2012**, *41*, 2740. (f) Wang, C.; Chen, J.; Talavage, T.; Irudayaraj, J. *Angew. Chem., Int. Ed.* **2009**, *48*, 2759. (g) Schladt, T. D.; Shukoor, M. I.; Schneider, K.; Tahir, M. N.; Natalio, F.; Ament, I.; Becker, J.; Jochum, F. D.; Weber, S.; Köhler, O.; Theato, P.; Schreiber, L. M.; Sönnichsen, C.; Schröder, H. C.; Müller, W. E. G.; Tremel, W. *Angew. Chem., Int. Ed.* **2010**, *49*, 3976. (h) Yuan, H.; Fales, A. M.; Vo-Dinh, T. *J. Am. Chem. Soc.* **2012**, *134*, 11358. (i) Schwartzberg, A. M.; Olson, T. Y.; Talley, C. E.; Zhang, J. Z. *J. Phys. Chem. B* **2006**, *110*, 19935. (j) Zhang, J. Z. *J. Phys. Chem. Lett.* **2010**, *1*, 686.

(4) (a) Haase, M.; Schäfer, H. *Angew. Chem., Int. Ed.* **2011**, *50*, 5808. (b) Wang, F.; Hao, Y.; Lim, C. S.; Lu, Y.; Wang, J.; Xu, J.; Chen, H.; Zhang, C.; Hong, M.; Liu, X. *Nature* **2010**, *463*, 1061. (c) Zhou, J.; Liu, Z.; Li, F. *Chem. Soc. Rev.* **2012**, *41*, 1323. (d) Wang, F.; Liu, X. *Chem. Soc. Rev.* **2009**, *38*, 976. (e) Wang, F.; Banerjee, D.; Liu, Y.; Chen, X.; Liu, X. *Analyst* **2010**, *135*, 1839. (f) Wang, Y.; Sun, L.; Xiao, J.; Feng, W.; Zhou, J.; Shen, J.; Yan, C. *Chem.—Eur. J.* **2012**, *18*, 5558. (g) Cheng, L.; Yang, K.; Li, Y.; Chen, J.; Shao, M.; Li, S.-T.; Liu, Z. *Angew. Chem., Int. Ed.* **2011**, *50*, 7385. (h) Wang, Z.; Hao, J.; Chan, H. L. W.; Wong, W.; Wong, K. *Small* **2012**, *8*, 1863.

(5) (a) Dong, B. A.; Xu, S.; Sun, J. A.; Bi, S.; Li, D.; Bai, X.; Wang, Y.; Wang, L. P.; Song, H. W. *J. Mater. Chem.* **2011**, *21*, 6193. (b) Yang, Y.; Shao, Q.; Deng, R.; Wang, C.; Teng, X.; Cheng, K.; Cheng, Z.; Huang, L.; Liu, Z.; Liu, X.; Xing, B. *Angew. Chem., Int. Ed.* **2012**, *51*, 3125. (c) Vetrone, F.; Naccache, R.; de la Fuente, A. J.; Sanz-Rodriguez, F.; Maestro, L. M.; Rodriguez, E. M.; Jaque, D.; Sole, J. G.; Capobianco, J. A. *ACS Nano* **2010**, *4*, 3254.

(6) Wang, F.; Deng, R.; Wang, J.; Wang, Q.; Han, Y.; Zhu, H.; Chen, X.; Liu, X. *Nat. Mater.* **2011**, *10*, 968.

(7) Han, W.; Yi, L.; Zhao, N.; Tang, A.; Gao, M.; Tang, Z. *J. Am. Chem. Soc.* **2008**, *130*, 13152. (b) Tian, Q.; Jiang, F.; Zou, R.; Liu, Q.; Chen, Z.; Zhu, M.; Yang, S.; Wang, J.; Wang, J.; Hu, J. *ACS Nano* **2011**, *5*, 9761. (c) Tian, Q.; Tang, M.; Sun, Y.; Zou, R.; Chen, Z.; Zhu, M.; Yang, S.; Wang, J.; Wang, J.; Hu, J. *Adv. Mater.* **2011**, *23*, 3542. (d) Zhou, M.; Zhang, R.; Huang, M. A.; Lu, W.; Song, S. L.; Melancon, M. P.; Tian, M.; Liang, D.; Li, C. *J. Am. Chem. Soc.* **2010**, *132*, 15351. (e) Hessel, C. M.; Pattani, V. P.; Rasch, M.; Panthani, M. G.; Koo, B.; Tunnell, J. W.; Korgel, B. A. *Nano Lett.* **2011**, *11*, 2560. (f) Han, S.; Gong, M.; Yao, H.; Wang, Z.; Yu, S. *Angew. Chem., Int. Ed.* **2012**, *51*, 6365.

(8) Verma, S.; Pravarthana, D. *Langmuir* **2011**, *27*, 13189.

(9) Lin, C. A.; Sperling, R. A.; Li, J. K.; Yang, T. Y.; Li, P. Y.; Zarella, M.; Chang, W. H.; Parak, W. J. *Small* **2008**, *4*, 334.

(10) Roper, D. K.; Ahn, W.; Hoepfner, M. *J. Phys. Chem. C* **2007**, *111*, 3636.

(11) (a) Gu, H.; Zheng, R.; Zhang, X.; Xu, B. *J. Am. Chem. Soc.* **2004**, *126*, 5664. (b) Lee, J. S.; Bodnarchuk, M. I.; Shevchenko, E. V.; Talapin, D. V. *J. Am. Chem. Soc.* **2010**, *132*, 6382.

(12) (a) Zhao, Y.; Pan, H.; Lou, Y.; Qiu, X.; Zhu, J.; Burda, C. *J. Am. Chem. Soc.* **2009**, *131*, 4253. (b) Luther, J. M.; Jain, P. K.; Ewers, T.; Alivisatos, A. P. *Nat. Mater.* **2011**, *10*, 361.

(13) Bjornerud, A.; Johansson, L. O.; Ahlstrom, H. K. *Magn. Reson. Med.* **2002**, *47*, 298.